Nanoscale

Accepted Manuscript

Volume 10
Number 4
28 January 2018
Pages 1549-2172

Nanoscale

rsc.li/nanoscale

ISSN 2040-3372

PAPER
Shuping Xu, Chongyang Liang et al.
Organelle-targeting surface-enhanced Raman scattering
(SERS) nanosensors for subcellular pH sensing

ROYAL SOCIETY
OF CHEMISTRY

NCNST

ROYAL SOCIETY
OF CHEMISTRY

rsc.li/nanoscale

Support Effect on Ni-Based Mono- and Bimetallic Catalysts in CO₂ Hydrogenation

Jihao Wang [1], Shilong Chen [1]*, Pierfrancesco Ticali [1], Paulina Summa [2], Simon Mai [1]，

Katarzyna Skorupska [2], Malte Behrens [1]*

[1] Institute of Inorganic Chemistry, Kiel University, Max-Eyth-Str. 2, 24118 Kiel, Germany

[2] Department of Inorganic Chemistry, Fritz-Haber-Institute of the Max-Planck-Society, Faradayweg

4-6, 14195 Berlin, Germany

*Corresponding authors, email: schen@ac.uni-kiel.de (S. Chen), mbehrens@ac.uni-kiel.de (M. Behrens)

Abstract

Aiming at a comprehensive understanding of support effects on Ni-based bimetallic catalyst for CO_2 hydrogenation, spectroscopy (DRIFTS) with CO as probe molecule and temperature-programmed techniques to investigate the impact of different supports (MgO, CeO_2, ZrO_2) on Ni- and Ni,Fe catalysts. Kinetic parameters revealed that the higher selectivity to methanation for Ni and Ni,Fe supported on the reducible oxides (CeO_2, ZrO_2) is due to the inhibition of reverse water-gas shift reaction (RWGS) by hydrogen. A promoting effect of Fe on Ni was only observed on MgO-supported catalysts. In situ DRIFTS with CO adsorption showed different electronic properties of Ni sites with partially reduced oxide (i.e. ZrO_2 and CeO_2). H_2-TPR and CO_2-TPD confirmed the significant role of metal-support interaction (MSI) in CeO_2-supported catalysts for CO_2 activation. The MSI between Ni / Ni,Fe and reducible supports are crucial for catalytic performance, ultimately leading to higher activity and stability in CO_2 hydrogenation.

Nanoscale Accepted Manuscript

1. Introduction

CO_2 hydrogenation is a cornerstone of sustainable "power-to-gas (P2G)" concepts[1-5] and supported Ni catalysts are considered as the most promising base metal catalyst towards methanation due to their outstanding catalytic performance and low cost.[6-10] Despite the long history of research on nickel-based catalysts, there is still need for a better fundamental understanding and for further rational optimization of such methanation catalysts.[11, 12]

One the one hand, regarding catalyst composition variation or promotion, partial substitution of Ni by a second metal was shown to improve the catalytic performance for CO_2 methanation.[13, 14] Compared to Ni catalysts, Ni,Fe bimetallic catalysts reach a significantly improved catalytic activity.[15-19] For example, Grunwaldt and co-workers reported that a small addition of Fe to Ni/Al_2O_3 catalysts will increase activity and stability with an optimum ratio of Ni: Fe = 3:1.[20-22] They proposed that the redox cycle of iron species on Ni nanoparticles will promote the dissociation of CO_2 and further improve the activity.[23] Similarly, Huynh *et al*. reported a Ni:Fe ratio of 4:1 to be optimal.[24] It was also reported that CO_2 is hydrogenated to HCOO* intermediates with a lower energy barrier. Meanwhile, other reports claim that the $Ni-FeO_x$ interfaces are more active for RWGS reaction due to its weak binding to CO* intermediates.[25]

On the other hand, CO_2 hydrogenation over supported Ni catalysts is highly structure-sensitive.[26-28] The size effect of Ni nanoparticles on CO adsorption has been proven to steer the selectivity of CO_2 hydrogenation, either to methane or to CO.[29, 30] In addition, the support also plays as an important role for Ni catalysts in CO_2 methanation,[31-36] including its impact on the size and shape of the Ni nanoparticles (i.e. dispersion and morphology),[37] but

also on CO_2 activation by the basicity and reducibility of the support.[38-40] Oxygen vacancies

can be formed in reducible oxides during CO_2 hydrogenation, affecting the catalyst behavior.

For example, in a series of Ni catalysts on different supports (Al_2O_3, ZrO_2, CeO_2), Ni

supported on non-reducible Al_2O_3 shown the lowest CO_2 conversion.[31] Furthermore, strong

metal-support interaction (SMSI) can affect the stability of CO_2 methanation, but also the

selectivity.[41] Such effects typically are dynamic and depend on the reaction conditions and

catalysts pre-treatments in a complicated manner. Monai *et al.* recently reported that such

SMSI can generate interfacial sites on Ni/TiO_2 catalysts favoring carbon-carbon coupling and

enhance the C_{2+} species formation during CO_2 hydrogenation.[42]

So far, the effect of reducible supports on bimetallic Ni,Fe catalysts for CO_2 hydrogenation

has not been studied to the same extent as the support effect on monometallic catalysts or the

Fe promotion effect on unreducible supports[43]. In this work, we first confirmed the intrinsic

optimal Ni:Fe ratio for methanation on non-reducible, but basic MgO. Then, monometallic Ni

and bimetallic Ni,Fe catalysts at this optimal ratio supported on MgO, ZrO_2 and CeO_2 have

been compared to study if the promotional effect of Fe depends on the varying reducibility of

the support by kinetic measurements, H_2-TPR, CO_2-TPD, and in situ DRIFTS measurements.

2. Experimental Section

2.1. Catalyst preparation

The catalysts were prepared by the incipient wetness impregnation method. For the support of

MgO, 1.25 mL of an aqueous solution containing $Fe(NO_3)_3 \cdot 9H_2O$ (99.5%, Grüssing GmbH)

and $Ni(NO_3)_2 \cdot 6H_2O$ (99.9%, abcr GmbH) was added dropwise to 1 g of MgO (>99%, Alfa

Aesar). The metal salt concentration was adjusted to reach a metal total (Ni and/or Fe)

loading of 5 wt.% on MgO. The wet powder was further stirred and then treated by

ultrasonication for 15 min. After drying at 80 °C overnight, the collected pre-catalysts were

directly reduced with 10 %H_2/N_2 at 450 °C for 2 h prior to the catalytic tests. By changing the

ratio between $Fe(NO_3)_3 \cdot 9H_2O$ and $Ni(NO_3)_2 \cdot 6H_2O$ in the aqueous solution, the molar ratio of

Ni:Fe has been adjusted to 1:0, 5:1, 2:1, 1:1, 1:2, and 0:1. The reduced samples are labelled

as Ni/MgO, Ni,Fe(83:17)/MgO, Ni,Fe(67:33)/MgO, Ni,Fe(50:50)/MgO, Ni,Fe(33:67)/MgO,

and Fe/MgO respectively. The same procedure has been applied to the supports of ZrO_2

(99%, Alfa Aesar) and CeO_2 (99.5%, Alfa Aesar), but only monometallic Ni and a Ni:Fe

ratio of 5:1 catalysts were selected, resulting in samples labelled as Ni/ZrO_2,

Ni,Fe(83:17)/ZrO_2, Ni/CeO_2 and Ni,Fe(83:17)/CeO_2.

2.2.Catalysts Characterization

Inductively coupled plasma optical emission spectroscopy (ICP-OES) was applied to analyze

the elemental compositions of those catalysts supported on MgO and CeO_2. The pre-catalysts

were dissolved in a mixture of nitric acid and hydrogen peroxide and measured on an Avio

200 ICP OES equipped with a S23 Autosampler (PerkinElmer). Due to the low solubility of

ZrO_2, the metal compositions of these catalysts were determined in a scanning electron

microscope by energy dispersive X-ray spectroscopy (SEM-EDX) using a Gemini

Ultra55Plus (Zeiss).

The surface area was measured by N_2 physisorption using the Brunauer–Emmett–Teller

(BET) method on a BELSORP MAX (Microtrac Retsch GmbH). The samples were

pre-treated at 100 °C for 2 h in vacuum to remove adsorbed moisture and air. The isotherm

was measured at -197 °C in liquid nitrogen.

Powder X-ray diffraction (PXRD) was used to study the crystal structure of the catalysts using Mo Kα radiation on a STADI P diffractometer (STOE). To avoid the re-oxidation of the reduced catalysts, the reduced samples were prepared in an Ar glovebox as sealed capillaries with 0.7mm diameter and later measured in the Debye-Scherrer mode.

Hydrogen temperature programmed reduction (H_2-TPR) was performed on a BELCAT II catalyst analyzer (Microtrac Retsch GmbH) to study the reducibility of the catalysts. The measurements were conducted with 50 mg of the samples filled in a quartz glass fixed-bed micro-reactor. After pretreatment at 120 °C under on Ar flow for 1 h, the reactor was cooled down to 40 °C and then heated to 1000 °C at a rate of 6 °C min^{-1} in a 50 sccm of 10 %H_2/Ar flow. The reactor was later kept at 1000 °C for 15 min before cooling down and the H_2 consumption was measured with a thermal conductivity detector (TCD). The degree of the reduction (%) of the supported metal was estimated by the H_2 consumption assuming that full reduction corresponds to a state with all Ni and Fe being metallic, CuO was used to calibrate the H_2 consumption.

CO_2 temperature programmed desorption (CO_2-TPD) profiles were recorded with the home-built reaction setup equipped with TCDs on the inlet and outlet of the quartz tube reactor. Prior the measurement, all samples were heated to 450 °C with a rate of 5 °C min^{-1} in a 10 mL min^{-1} of 20% H_2/Ar flow. After an isothermal reduction at 450 °C for 2 h, samples were cooled down to 50 °C in a flow of He to remove the residual gases from the reduction. CO_2 adsorption was carried out at 50 °C for 2 h with a flow rate of 10 mL min^{-1}. Then a 10 mL min^{-1} of He was introduced to remove physically adsorbed CO_2 before the desorption. CO_2-TPD curve was drawn at the temperature range from 50 to 600 °C with the heating rate

of 10 °C min⁻¹. The number of surface basic sites was calculated using the integration of the calibrated CO_2 peak below the curve. The raw data were smoothed first and then fitted (Figure S3, SI) into three Gaussian peaks at different temperature ranges representing the weak, medium and strong basic sites.

Transmission Electron Microscopy (TEM) was employed to evaluate the nanoparticle size of the freshly reduced samples. TEM images were taken in the bright field mode on a Tecnai F30 G2 S-TWIN (Thermo Fisher Scientific) equipped with a field emission gun (FEG) using an acceleration voltage of 300 kV and a spherical aberration coefficient of 1.2 mm. Due to the low metal loading and small nanoparticle size, the brightness and contrast of TEM images were adjusted to clearly identify metal particles.

Diffuse Reflectance Infrared Fourier Transform Spectroscopy (DRIFTS) measurements were performed on the reduced catalyst following the adsorption and desorption of CO used as a probe molecule. The samples were heated up to 450 °C with 5 °C min⁻¹ in an 80 mL min⁻¹ flow of 10%H_2/He and then an isothermal reduction was performed for 2 h. Afterwards, the reduced catalysts were purged in pure He for 30 min and then cooled down to 10 °C. The analysis was performed under 80 mL min⁻¹ of 0.5 % CO/He mixture flow for 40 minutes during adsorption and pure He flow for 40 minutes during desorption. The spectra were collected by a *iS50* FTIR spectrometer (Thermo Fisher Scientific) equipped with a high-temperature reaction chamber (Praying Mantis, Harrick) coupled with a dome mounting ZnSe windows. All measurements were collected by the *OMNIC* software via an automatic series collection using a Gram-Schmidt method. The temperature was controlled by *Harrick ATC* and a *Huber Ministat 125* chiller. No compensation of H_2O and CO_2 signal was used.

2.3. Kinetic measurements

Catalytic tests were performed in a U-shaped micro-reactor where the catalyst bed was fixed by quartz wool plugs. A thermocouple was inserted directly into the catalyst bed to measure the temperature. After isothermal reduction at 450 °C for 2 h, the reactor was cooled down to 350 °C and 50 sccm of a reaction gas mixture was injected into the reactor to start the CO_2 hydrogenation test at atmospheric pressure, consisting of 9.6% CO_2/N_2, 38.4% H_2 and balanced N_2. The inlet gas flow was controlled by mass flow controllers (Bronkhorst) and the gas composition at the exhaust was evaluated by a micro-GC (INFICON). In a typical catalytic test, 30 mg of MgO-supported catalysts were used while 10 and 3 mg of the ZrO_2 and CeO_2-supported catalysts were sufficient to reach a similar CO_2 conversion of less than 25% to ensure the measured selectivity for methanation can be compared at similar conversion levels. The catalyst sieve fraction of 200~300 μm was diluted with 350~460 μm SiC (Thermal Scientific) to give a total weight of 200 mg to avoid heat and mass transfer issues.

The activation energies (E_a) of selected catalysts were measured at temperatures ranging from 315 to 355 °C and reaction orders for H_2 and CO_2 were tested in the same reactor at 350 °C by changing the respective partial pressures. All the kinetic measurements were conducted under low CO_2 conversion of less than 25%.

As shown in eq. (1), the reaction rates of CO_2 hydrogenation were defined as the CH_4 production rate (r_{CH4}) for methanation and the CO production rate (r_{CO}) for the RWGS normalized to the weight of active metals. The conversion of CO_2 and the selectivity for

CH_4/CO were calculated as eq. (2) and (3).

$$r_{CH4/CO} = \frac{Flow\ rate\ \times conc._{CH4/CO}}{g_{cat.} \times wt.\%} \qquad eq.(1)$$

$$Conv._{CH4/CO} = 1 - \frac{conc._{CO2,out}}{conc._{CO2,in}} \qquad eq.(2)$$

$$Selec._{CH4/CO} = \frac{conc._{CH4/CO}}{conc._{CH4/CO} + conc._{CO/CH4}} \qquad eq.(3)$$

3. Results

The metal loading of the as-synthesized samples was checked by ICP-OES and SEM-EDX, which confirmed the total metal loading are approximately $5_{wt.}\%$ for all the samples (Table S1-2, Supporting Information (SI)). For the bimetallic catalysts, also the measured Ni:Fe ratios are in reasonable agreements with the nominal values (Table S1-2, SI). The BET surface areas of the commercial supports are approximately 15 (MgO), 26 (ZrO_2), and 64 (CeO_2) m^2g^{-1} (Table S3, SI). The reducibility of the Ni,(Fe)/MgO catalysts was studied by H_2-TPR (Figure 1a). With increasing Fe content, the reduction peaks gradually shift to higher temperatures. Such trend is consistent with previous reports and can be explained by the less noble nature of iron compared to nickel.[44, 45] A single TPR peak was observed for the reduction into the metallic state indicating presence of uniform metal species.[46, 47] Only a weak shoulder is observed at the lower temperature side of the TPR profile (around 400 °C) with increasing Fe content, which can be assigned to the intermediate reduction of Fe^{3+} to Fe^{2+}.[47-49] There is no significant reduction at temperatures higher than 500 °C for all the MgO-supported catalysts confirming the unreducible nature of the support at these conditions. Thus, an isothermal reduction at 450 °C for 2 h was chosen to reach a full reduction of both Ni and Fe. The XRD patterns of the freshly reduced samples are shown in Figure 1b. The major crystalline phase in all catalysts is MgO while there are no obvious

reflections of Ni or Fe metal detected, which can be explained with the low loading of active
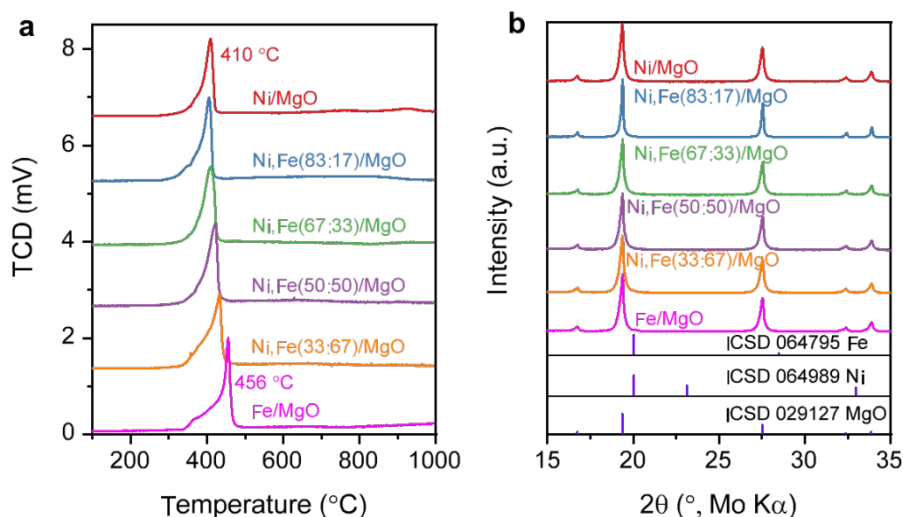
metal and the small crystallite size.

Figure 1. a H_2-TPR profile for Ni,Fe monometallic and bimetallic catalysts supported on MgO and **b** their PXRD patterns after isothermal reduction of 450 °C.

The catalytic performance of the reduced Ni,Fe/MgO catalysts for CO_2 hydrogenation was

evaluated at 350 °C for 16 h after the above-described reduction step. Both of the

monometallic Ni and Fe catalysts showed stable activity in methanation and RWGS (Figure

2) and, as expected, Ni had a higher activity and selectivity to methane. Note that it was

reported that the addition of low amounts of Fe to Ni catalysts can prohibit the deactivation of

monometallic Ni catalyst,[22, 50] but no such deactivation was present for the MgO-supported

monometallic Ni in our experiment. However, the bimetallic Ni,Fe catalysts showed high

CO_2 conversions at the beginning, but suffer from gradual deactivation over 16 h time on

stream (TOS). In this process, methanation deactivated stronger than RWGS leading to a

decrease of CH_4 selectivity (Figure 2b~d). Sintering and carbon deposition are the most

probable reasons for such initial deactivation.[51-53] Under methanation reaction conditions, it

has been reported that small Ni nanoparticles may coalesce to form bigger particles, followed by the Ostwald ripening.[54, 55] The particle size growth can also be associated to the formation of metal carbonyls due to the enhanced mobility of $Ni(CO)_x$ species.[55-57] The particle size increase will result in the loss of surface area and active sites, eventually resulting in the deactivation of catalysts. After 16 h TOS, both the methanation and RWGS rates have approached to a steady-state for each catalyst, revealing a volcano-shaped trend with the Fe loading (Figure 3). The optimal Ni:Fe ratio for the CO_2 hydrogenation was identified as 5:1, i.e. Ni,Fe(83:17)/MgO, with the highest activity in both methanation (0.035 $mmol_{CH4}$ g^{-1}_{metal} s^{-1}) and RWGS (0.302 $mmol_{CO}$ g^{-1}_{metal} s^{-1}). It was proposed that iron oxide species can be formed from the oxidation of iron by CO_2 and H_2O in the gas stream. These can be dispersed on the Ni particles, and the redox cycle of oxidized Fe species can promote the CO_2 hydrogenation.[20-23] A similar dynamic promotion effect in Co,Fe bimetallic catalysts in CO_2 hydrogenation was interpreted as a result of alloy formation after reduction of bimetallic catalysts.[58] In both scenarios, a too strong increase in Fe loading will cause either blocking or substitution of active Ni sites at the surface, which explains the decreased activity with higher Fe loading, which is not uncommon for promoter species. Besides, our Ni,Fe bimetallic catalysts also suffer from deactivation, which might be associated with the gradual and dynamic formation of such oxidized Fe "islands".

The Ni,Fe(83:17)/MgO catalyst reached the highest reaction rate of both methanation and RWGS reactions with the highest CH_4 selectivity in this series of catalysts (~10.2 %) (Figure 2b-d). This ratio of 5:1 for Ni:Fe has been employed in the study of the other two supports, i.e. ZrO_2 and CeO_2, to investigate the support effect on the Ni,Fe bimetallic catalysts for CO_2
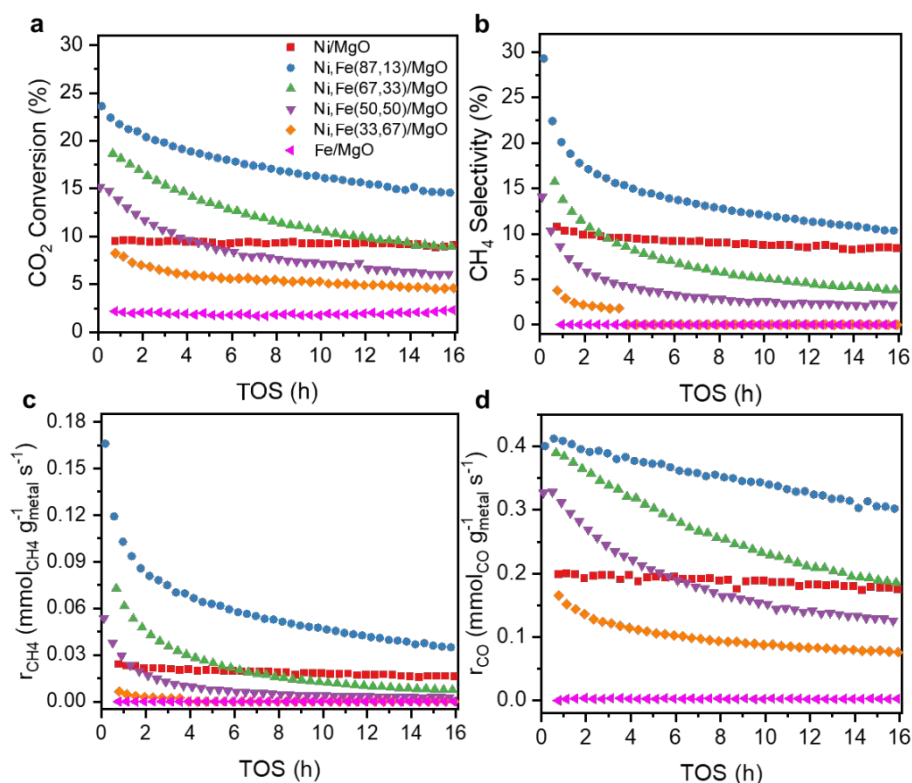
hydrogenation.

Figure 2. a CO_2 conversion, **b** selectivity towards CH_4, **c** methanation rate and **d** RWGS rate as a function of TOS for MgO-supported catalysts with various Ni:Fe ratios at 350 °C.
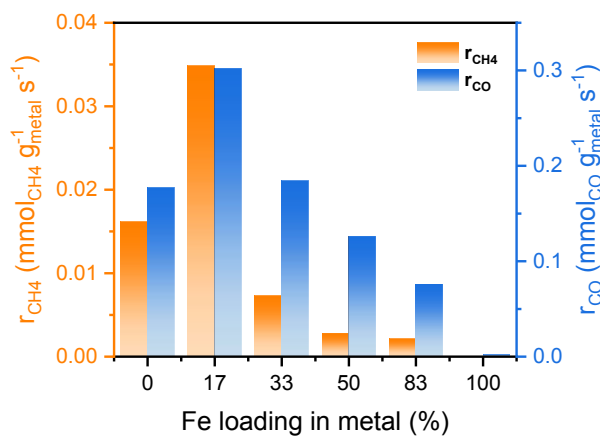

Figure 3. Reaction rates of both methanation and RWGS after 16 h test for different Fe loadings in Ni,(Fe)/MgO catalysts.

The reducibility of these two series catalysts was studied first. The H_2-TPR profiles of ZrO_2

and CeO_2 supported catalysts exhibit two reduction peaks below 400 °C, which could result

from weakly and strongly bound Ni^{2+} and Fe^{3+} species[59, 60] (Figure 4a), indicating the

reduction of the metal completes before 450 °C. Besides, the reduction degree (%) of the

supported metal estimated by the H_2 consumption assuming that all Ni and Fe can be fully

reduced were compared among these mono- and bimetallic supported catalysts, following the

order CeO_2- > ZrO_2- > MgO-supported catalysts (Figure 4c). The higher reduction degree of

CeO_2- and ZrO_2-supported catalysts agree with the reducibility of these oxides. For the

CeO_2-supported catalysts, reduction degree even higher than 100 % clearly indicate that

support species have been reduced together with the metal oxide species at low temperature

(< 300 °C), agreeing well with the previous report of co-reduction of highly dispersed metal

and support-CeO_2,[61-63] which was explained by metal-support interaction (MSI) and / or
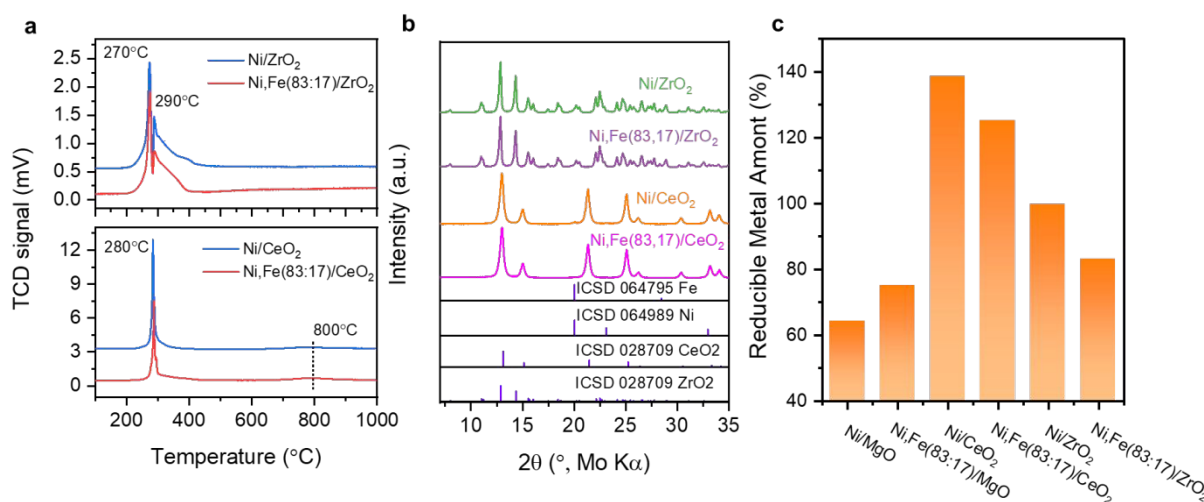
hydrogen spillover effects.[64-68]

Figure 4. a H_2-TPR profile for Ni monometallic and Ni,Fe bimetallic catalysts supported on ZrO_2, CeO_2; **b** the PXRD patterns of the samples reduced isothermally at 450 °C and **c** the estimated degree of reduction, where valued beyond 100% refer to co-reduction of support species.

The XRD patterns of these reduced samples show broad reflections for Ni and Fe at around

20 °2θ, which might be due to the small metal particle size or low metal loading (Figure 4b).

The broad XRD peak profiles agree well with the TEM images showing that most metal nanoparticles have a size around 5~10 nm (Figure 5). Similar nanoparticle sizes were found for all six catalysts, which indicates that the comparison here is not strongly affected by possible size effects on CO_2 hydrogenation.[69]
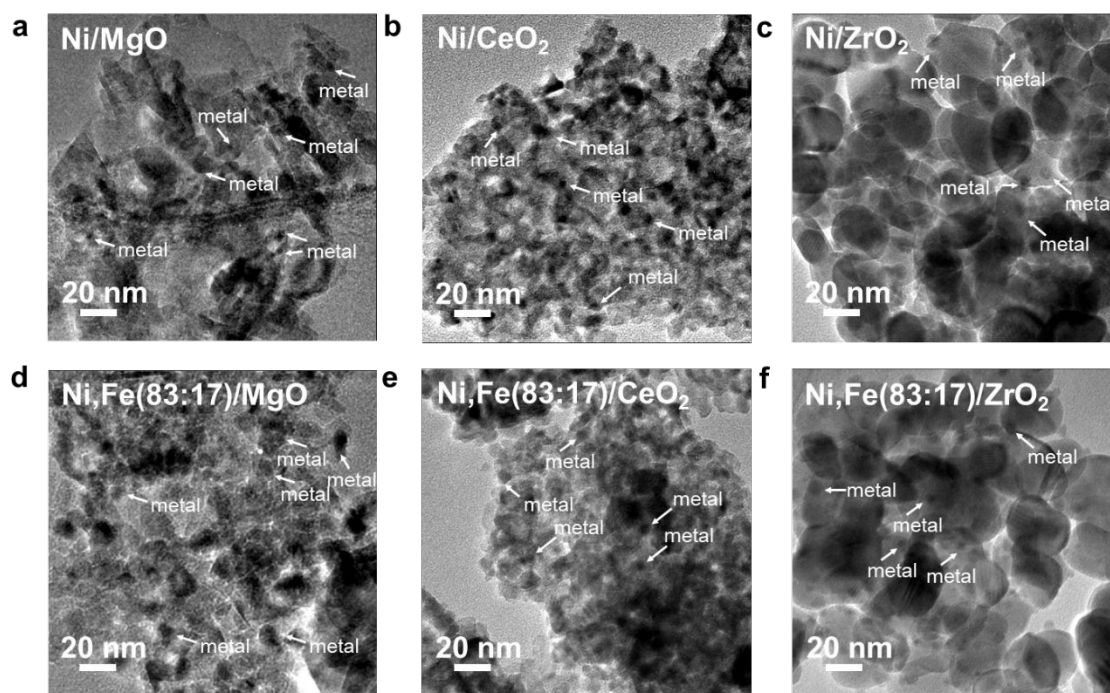
Figure 5. TEM images for Ni-Fe monometallic and bimetallic catalysts supported on **a&d** MgO, **b&e** ZrO_2 and **c&f** CeO_2.

All supported Ni and Ni,Fe(83:17) catalysts were studied in the CO_2 hydrogenation reaction at 350 °C for 16 hrs. The CO_2 conversion is similar for monometallic Ni and bimetallic Ni,Fe(83:17) catalysts on both supports ZrO_2 and CeO_2, suggesting in contrast to MgO-supported catalysts, no clear promotion effect of Fe on the CO_2 conversion for these reducible supports (Figure S2, SI). Monometallic Ni even showed a higher CO_2 methanation rate than bimetallic Ni,Fe(83:17) if supported on ZrO_2 or CeO_2 (Figure 6) showing a negative effect of Fe addition on the methane selectivity. Actually, Winter *et al*. already found that the

introduction of Fe to Ni catalysts supported on CeO_2 will increase the selectivity towards RWGS.[70] They proposed that the formation of oxidized Fe will weaken the CO binding strength, resulting in desorption. Since the adsorbed CO is one of the potential intermediates for methanation, this can explain the lower selectivity to CH_4 in favor or RWGS.[71] However, this is very different to MgO-supported catalysts where the addition of Fe enhances both CO_2 conversion and methane selectivity, though on a lower level of around 10%. The absolute selectivity to methane for Ni/CeO_2 and Ni/ZrO_2 were much higher than on MgO and reached 82.3 % and even 94.4%, indicating that the methanation reaction is greatly promoted by the reducible nature of the oxide support with a much stronger effect than the presence or absence of Fe.

While the selectivity remains quite stable during the 16 hours TOS (Figure 6), the conversions show an interesting trend (Figure S2, SI). The CeO_2-supported catalysts show a slight deactivation, which is much less pronounced compared to Ni,Fe(83:17)/MgO, but for the ZrO_2 supports, a clear activation phase in both of methanation and RWGS reactions was observed. A similar behavior was found before in Ru/ZrO_2 in CO_x methanation,[39, 72] which was explained by the slow reduction of ZrO_2 leading to increasing metal-support interaction during the hydrogenation reaction.

The reaction pathways on Ni/ZrO_2 and Ni/CeO_2 catalysts discussed in the literature indeed assume a strong involvement of the support. CO_2 is first adsorbed on a hydroxyl group of the ZrO_2 / CeO_2 support. There, it can be hydrogenated to formate by dissociated hydrogen from metallic Ni under desorption of H_2O.[73-77] The formate intermediate can either decompose and then transfer onto the surface of the metallic Ni nanoparticle or directly be converted on the

ZrO_2 / CeO_2 surface to CH_4 by combing with more dissociated hydrogen spilled over from Ni.[73, 75-77] Both reaction pathways require a strong participation of ZrO_2 / CeO_2 in the CO_2 activation steps. The latter pathway even avoids adsorption of any carbon- or oxygen-bound intermediates on the surface of Ni, which could help to keep the metallic Ni particles free from deactivating species. Contrarily, for the catalysts supported on MgO, CO_2 and its CO* or HCOO* intermediates may absorb mainly on the Ni surface, which increases the probability of strong deactivation by oxidation or coking.[7]

Comparing the steady-state activity (after 16 h TOS) among these Ni and Ni,Fe catalysts supported on three different oxides, the CeO_2 supported catalysts show the highest activity. Ni/CeO_2 has the highest methanation rate of 3.0 $mmol_{CH4}$ g_{metal}^{-1} s^{-1} and $Ni,Fe(83:17)/CeO_2$ has the highest RWGS rate of 1.3 $mmol_{CO}$ g_{metal}^{-1} s^{-1} (Figure 7). The steady-state activity of the methanation reaction followed the order of MgO-supported < ZrO_2-supported < CeO_2-supported, which agrees well with the reducibility order: MgO < ZrO_2 < CeO_2 and underlines to role of a SMSI or electronic metal-support interaction (EMSI) effect.[18, 33, 39, 78]

The basicity of the Ni-based monometallic catalysts and their bare support were investigated through CO_2-TPD experiments (Figure 8, Table 1). CO_2-TPD profiles revealed three Gaussian peaks representing the weak (100-170 °C), medium (222-302 °C), and strong (396-501 °C) basic sites. The low-temperature peak corresponds to the CO_2 desorption from weak Brønsted sites.[79-82] The medium-temperature peak originates from bidentate carbonates on metal–oxygen pairs such as Mg-O.[79-82] The high-temperature peak is correlated to the desorption of unidentate carbonates on low-coordination O^{2-} anions.[79-83] Based on the quantitative analysis of CO_2-TPD profiles, Ni/CeO_2 catalysts have the highest content of

weak basic sites (29 $\mu mol_{CO2}/g_{cat}$) among these three supported Ni catalysts, which indicates that the CeO_2 support can facilitate the CO_2 adsorption, contributing to its high activity. [84-86]

Furthermore, compared to the bare support, our results suggest that CeO_2-supported catalysts have a higher total density of basic sites (85 $\mu mol_{CO2}/g_{cat}$ for Ni/CeO_2 *vs.* 54 $\mu mol_{CO2}/g_{cat}$ for CeO_2), whereas a lower total basic sites density was observed for the MgO-supported (111 $\mu mol_{CO2}/g_{cat}$ for Ni/MgO *vs.* 167 $\mu mol_{CO2}/g_{cat}$ for MgO) and ZrO_2-supported (26 $\mu mol_{CO2}/g_{cat}$ for Ni/ZrO_2 *vs.* 85 $\mu mol_{CO2}/g_{cat}$ for ZrO_2) samples. Notably, experimental results have revealed that MgO and its catalysts release significantly more CO_2 during the TPD experiments. This increased CO_2 release is likely related to the presence of bulk carbonates formed during CO_2 adsorption[87, 88] and is not necessarily indicative of surface basicity. Nevertheless, these results clearly demonstrate that the SMSI in Ni/CeO_2 catalyst results in interfacial sites more favorable for CO_2 activation / conversion. As Ni/CeO_2 contains a higher density of basic sites than the bare support CeO_2, and given than the density of basic sites can be correlated to the oxygen vacancy density, this is consistent with the results of the H_2-TPR analysis. [89, 90]
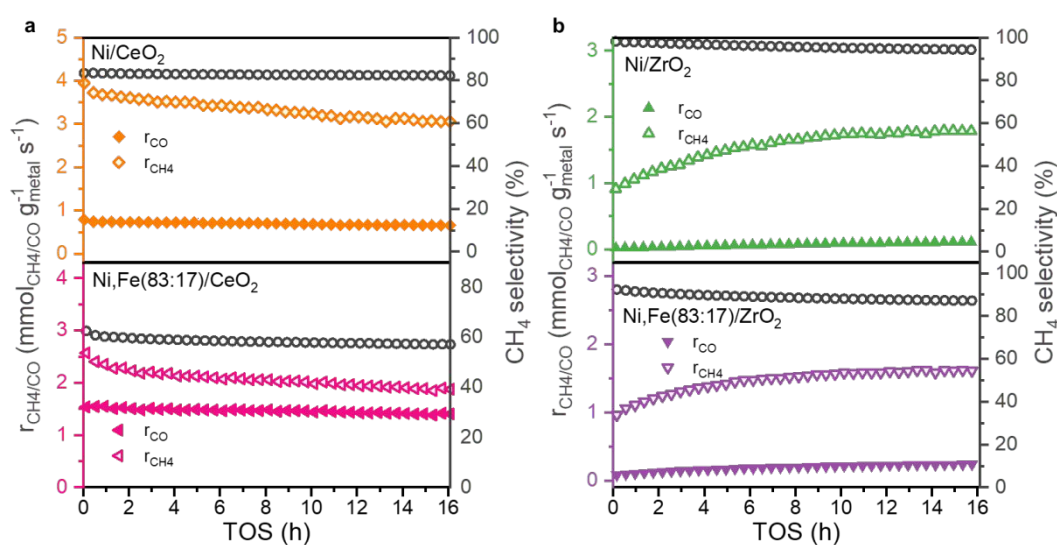
Nanoscale Accepted Manuscript

Figure 6. Methanation and RWGS rates and selectivity towards CH_4 as a function of TOS for **a** CeO_2 and **b** ZrO_2-supported monometallic and bimetallic catalysts for 16 h TOS at 350 °C.
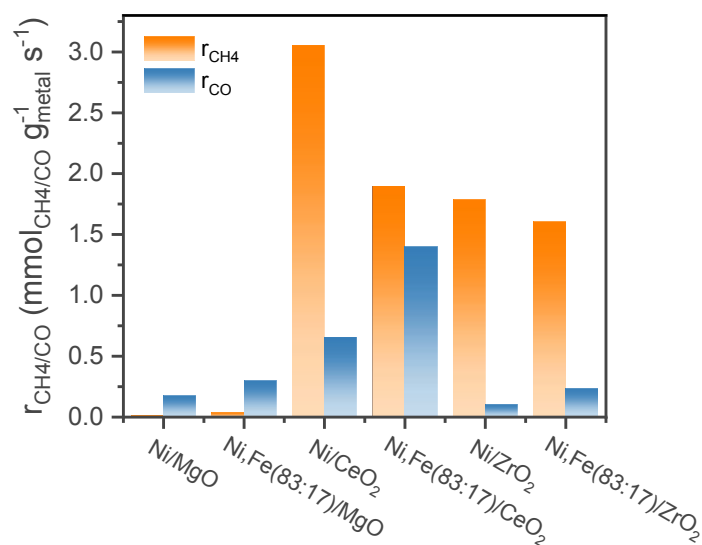

Figure 7. Comparison of the reaction rates of the different supported mono- or bimetallic catalysts for both methanation and RWGS after 16 h TOS.
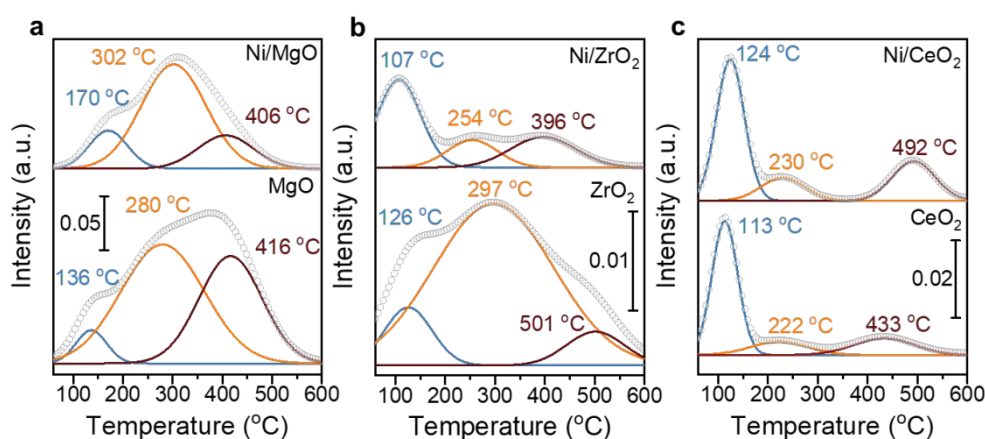

Figure 8. CO_2-TPD profiles at 10 °C min^{-1} for **a** MgO, **b** ZrO_2, **c** CeO_2 supports, and their corresponding Ni loaded catalysts where grey dots represent the smoothed raw profiles and the solid color lines indicate the fitting results for week, medium and strong basic sites at different temperatures

Table 1. Calculated basic site density based on the results from CO_2-TPD of the bare supports and the reduced catalysts

	Weak [μmol/g]	Medium [μmol/g]	Strong [μmol/g]	Total [μmol/g]
MgO	15	87	65	167
Ni/MgO	17	72	21	111
ZrO_2	11	52	22	85
Ni/ZrO_2	12	7	7	26
CeO_2	27	8	19	54

Ni/CeO$_2$	29	19	37	85

Further kinetic experiments were conducted for Ni and Ni,Fe catalysts to determine the apparent activation energy (E_a) and reaction order of CO_2 and H_2 with respect to methanation and RWGS for a deeper investigation of the support effect. From the Arrhenius plot shown (Figure 9a-c), the apparent activation energy E_a for MgO and CeO$_2$ supported catalysts are very similar between 71 and 79 kJ mol^{-1} in both methanation and RWGS reactions. However, the intercepts in the Arrhenius plot for the MgO-supported catalysts are much lower than for the CeO$_2$-supported catalysts, suggesting more actives sites from the latter catalysts. This interpretation agrees with the previous hypothesis that the metal-support interaction provides additional abundant active sites at the ceria-metal interfaces. Besides, the high reducibility of CeO$_2$ results into more oxygen vacancies introducing the so-called electronic metal-support-interaction (EMSI) effect, which can activate CO_2 at lower temperatures.[18] For ZrO$_2$-supported catalysts, the Arrhenius plots suggest a different activation energy compared to MgO- and CeO$_2$-supported catalysts. Here, the E_a of methanation is 94.4 kJ mol^{-1}, which is almost half of that of RWGS (196.6 kJ mol^{-1}), implying that the relative barrier energy for RWGS is very high on this type of catalyst. The big difference in activation energy for these two reactions on Ni/ZrO$_2$ can account for the highest methane selectivity for ZrO$_2$-supported catalysts.
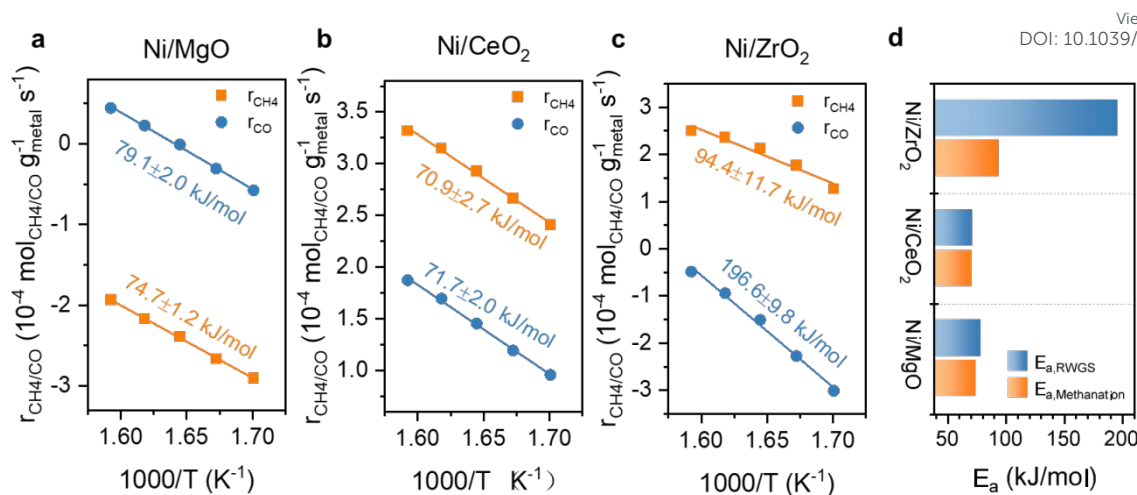
Nanoscale Accepted Manuscript

Figure 9. Arrhenius plots with calculated E_a for Ni catalysts supported on **a** MgO, **b** CeO$_2$, **c** ZrO$_2$ and **d** comparison of their E_as for RWGS and methanation.

The reaction orders of CO$_2$ and H$_2$ for monometallic Ni and bimetallic Ni,Fe catalysts were studied for understanding of the limiting factors of reactants activation (Figure 10-11). For the three monometallic Ni catalysts, an increasing in CO$_2$ partial pressure affected the RWGS more than methanation, suggesting that the RWGS is limited by the activation of CO$_2$, especially for Ni/CeO$_2$ with the highest CO$_2$ reaction order of 1.08 in RWGS (Figure 10a-c). At the same time, the H$_2$ partial pressure variation affected the methanation rate stronger and positively showing that the methanation is rather limited by the activation of H$_2$. The RWGS was even affected negatively by an increase in the H$_2$ partial pressure for the two catalysts on the reducible supports, CeO$_2$ and ZrO$_2$, especially for ZrO$_2$-supported catalysts with a value of -0.86 (Figure 10d-f). The high selectivity towards CH$_4$ for the ZrO$_2$-supported catalysts can therefore also be explained by the hydrogen-rich condition (H$_2$:CO$_2$ = 4:1), which also agrees well with the previous results of activation energy. In addition, as the calculated reduction degree of CeO$_2$ supported catalysts exceeds 100 %, indicating that not only Ni and Fe were activated to the metallic state, but CeO$_2$ was also partially reduced to CeO$_{2-x}$, forming surface oxygen vacancies.[91, 92] The oxygen vacancies donate electrons which could

participate in the adsorption and activation of CO_2, explaining the reason that the CeO_2 supported catalysts with relatively rich oxygen vacancies have a higher CO_2 reaction order in both methanation and RWGS (Figure 10). Furthermore, the H_2-spillover effect is supported by the H_2-TPR result where the reduction of surface CeO_2 occurs at around 280 °C, significantly lower than the surface reduction temperature of pure CeO_2, which is normally around 450 °C.[62, 93, 94] This indicates that the dissociated H migrate from the metal to the metal-support interface and can hydrogenate the activated CO_2.
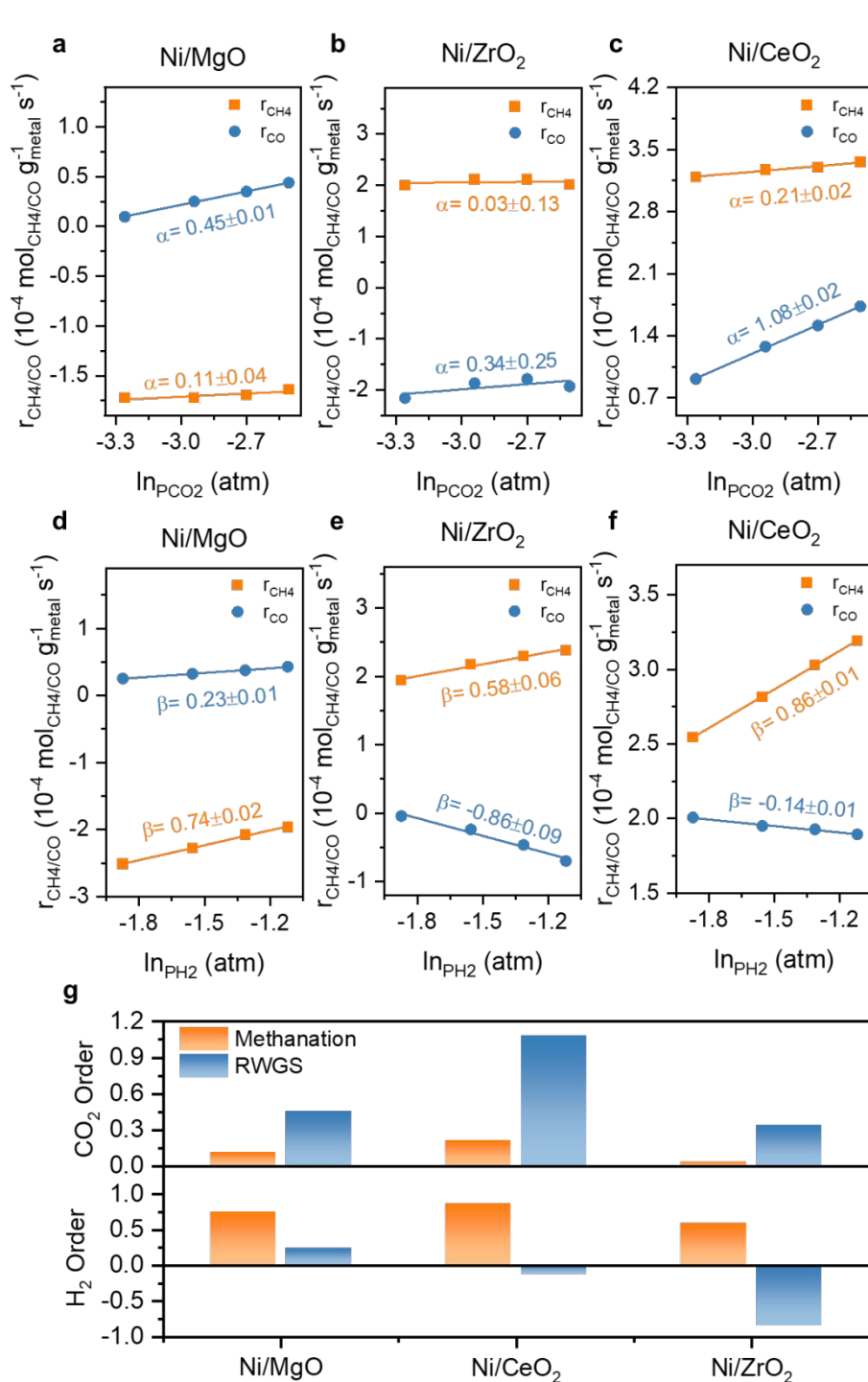
Figure 10. The reaction order of CO_2 (α) and H_2 (β) at 350 °C for Ni monometallic catalysts supported on **a&d** MgO, **b&e** ZrO_2 and **c&f** CeO_2 and **g** their comparison.

The reaction orders of CO_2 and H_2 for the bimetallic Ni,Fe catalysts are shown in Figure 11.

Compared to the monometallic catalysts, there was a more significant increase in both

reaction orders of CO_2 and H_2 for methanation compared to RWGS reaction on the

MgO-supported catalyst, corresponding to the higher methanation selectivity on the

bimetallic catalysts (Figure 2). For the ZrO_2-supported catalyst Ni,Fe(83:17)/ZrO_2, the H_2

reaction order of -0.21 in RWGS was still negative but has increased strongly from -0.86

observed in Ni/ZrO_2. This less negative H_2 reaction order showed that the H_2-inhibition of

RWGS was mitigated compared to the monometallic Ni catalyst, consistent with a lower

RWGS selectivity on this bimetallic catalyst (Figure 6b). Notably, introducing Fe to Ni/CeO_2

minorly modified the reaction order of CO_2 or H_2 in both methanation and RWGS.
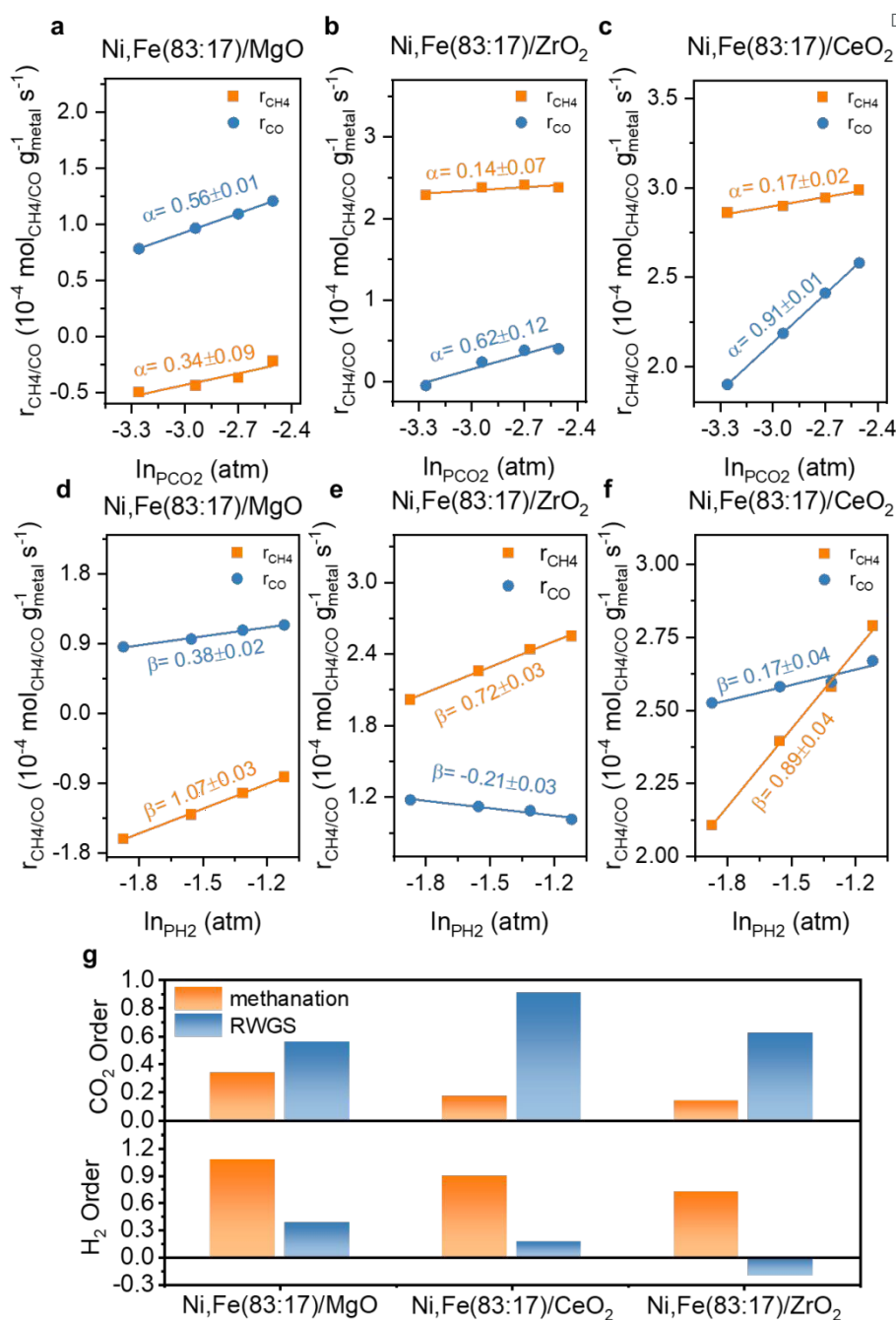
Figure 11. The reaction order of CO_2 (α) and H_2 (β) at 350 °C for Ni,Fe bimetallic catalysts supported on **a&d** MgO, **b&e** ZrO_2 and **c&f** CeO_2 and **g** their comparison.

Additionally, *in situ* DRIFTS combined with CO as a probe were performed on the Ni monometallic catalysts to study the impact of the support on the surface properties of Ni. The formed surface species during CO adsorption can be divided in two main regions: one with spectral features above 1800 cm^{-1} and the other with features below 1800 cm^{-1}. For Ni/MgO,

the spectra region above 1800 cm^{-1} is characterized by adsorbed CO (CO$_{ad}$) species i.e. the metal carbonyl, in particular the linear Ni^0-CO species (2056 and 2029 cm^{-1}) and the bridged (Ni^0)$_x$-CO species (1945 and 1919 cm^{-1}).[95-97] At features below 1800 cm^{-1}, several bands can be identified as carbonate, bicarbonate, and formate species.[96, 98-100] The intensity of carbonaceous / carbonate-like species and CO$_{ad}$ species increased as a function of the CO adsorption time (Figure 12a). In the desorption period (Figure S4, SI), CO$_{ad}$ species gradually diminished and left a bit amount of CO$_{ad}$ adsorbed on the Ni surface while carbonate, bicarbonate, formate species region remained after 40 min of desorption.
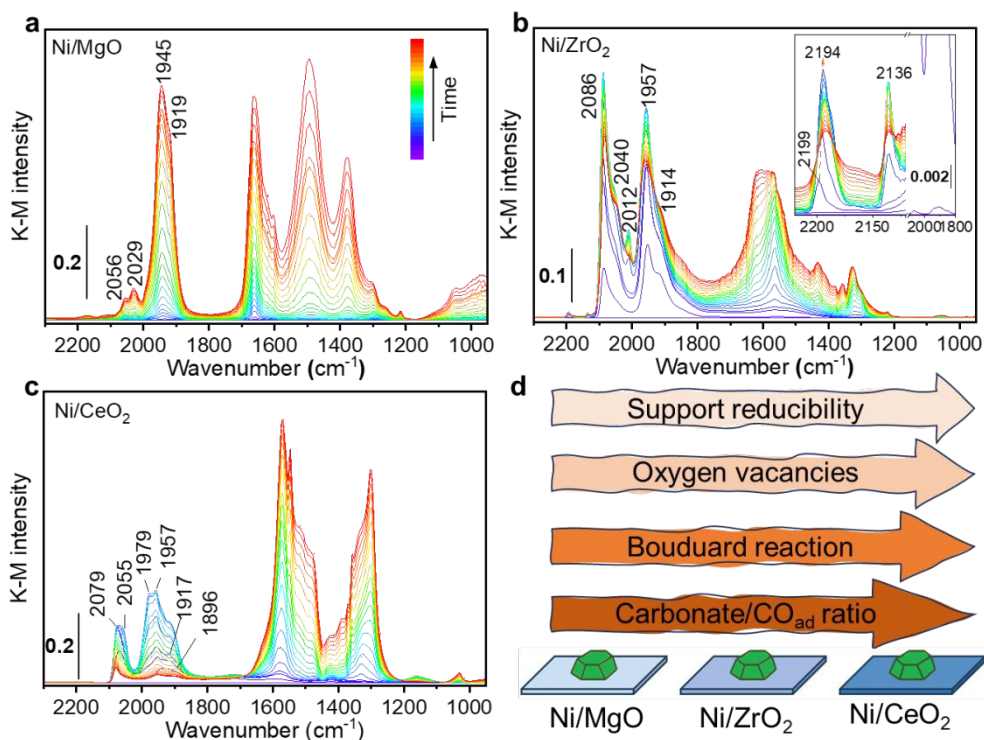
Figure 12. *In situ* DRIFTS spectra of **a** Ni/MgO, **b** Ni/ZrO$_2$ and **c** Ni/CeO$_2$ catalysts collected during CO adsorption, inset images in **b** representing the zoom-in spectra at features above 2100 cm^{-1}. Illustration **d** of the structural properties changes in three different supported Ni Catalysts.

For Ni/ZrO$_2$, CO adsorption resulted in the formation of a very intense peak at 2086 cm^{-1}, with a shoulder at 2040 cm^{-1}, which was ascribed to linear Ni^0-CO (Figure 12b). At higher frequency, two tiny peaks were identified and ascribed to linear Ni^{2+}-CO (2199-2194 cm^{-1})

and Ni^+-CO (2136 cm^{-1}).[97] Besides, the two bands at 1957 and 1914 cm^{-1} were ascribed to bridged $(Ni^0)_X$-CO species. In the lower frequency region below 1800 cm^{-1}, several bands were observed and identified as carbonate and bicarbonate species, similar to Ni/MgO. During the CO adsorption, the intensity of all CO_{ad} bands increased to a maximum after about 6 minutes and then started to decrease. Meanwhile, a continuous increase in the range of the carbonaceous / carbonate-like species bands was observed. This change of the intensity was interpreted as Boudouard reaction ($2 CO \rightarrow CO_2 + C$) on the active sites of Ni.[101]

The disproportionation of CO to carbon would result in the partial encapsulation of some Ni sites and a lower intensity for CO_{ad} species. Meanwhile, the produced CO_2 can be adsorbed and formed the carbonate species on the adjacent ZrO_2. Note that one cannot exclude a direct CO adsorption contributing to the formation of carbonaceous / carbonate-like species as described for Ni/MgO. In the desorption process, except for the bands of ionic Ni^{n+}-CO species, almost all the bands are stable and still present during purging in He (Figure S5, SI). Only the linear Ni^0-CO species lost more than half of its intensity, suggesting the presence of less stable Ni^0-CO species.

Regarding the Ni/CeO$_2$ catalyst, CO adsorption led to the formation of the similar species observed for Ni/MgO: linear Ni^0-CO (2079 and 2055 cm^{-1}) and bridged $(Ni^0)_x$-CO (1979, 1957, 1917 and 1896 cm^{-1}) species.[97] Various carbonate-like species bands were observed and were ascribed to the CeO$_2$ support in the frequency region lower than 1800 cm^{-1}. In the CO adsorption process, similarly to the Ni/ZrO$_2$ sample, a change of the CO_{ad} species intensity was observed. This behaviour becomes even more remarkable on Ni/CeO$_2$ than Ni/ZrO$_2$, with a major intensity reduction that drastically reduces the intensity of all CO_{ad}

species. Such behaviour could be related to the stronger reducibility of CeO_2 than ZrO_2, which was also proved by the H_2-TPR results (Figure 4). Compared to Ni/ZrO_2, more oxygen vacancies of Ni/CeO_2 formed during reduction pre-treatment (proved by H_2-TPR) drove a more pronounced charge transfer between Ni and reduced CeO_2 (EMSI effect), resulting in a higher electron density on Ni sites in Ni/CeO_2 catalyst, which leads to a more active CO disproportionation (Figure 12d). Such concept that charge transfer from oxygen vacancies to adjacent metal sites through EMSI effect has been also demonstrated on Ru/ZrO_2 catalysts both in experimental and theoretical aspects.[72] Moreover, the formation of carbon layer on the top of Ni^0 sites during disproportionation would inhibit the further adsorption of CO molecules. Such hypothesis is consistent with the observation that the intensity of CO_{ad} species were much lower than the carbonate bands on Ni/CeO_2 catalyst (Figure 12c). During the desorption process, almost all CO_{ad} species disappeared (Figure S6, SI), suggesting a very labile nature of these species and influenced by a stronger electron density transferred from the reduced CeO_2 support. At the same time, the carbonaceous /carbonate-like species slightly increased in intensity, indicating that some CO molecules could have been re-adsorbed to form carbonaceous /carbonate-like species after being desorbed from Ni^0 sites.

4. Discussion

The support effect on the Ni,Fe bimetallic catalysts as well as Ni monometallic catalysts in CO_2 hydrogenation (methanation and RWGS) studied here can be summarized and interpreted as follows:

1. On a series of Ni-based (Ni,Fe) catalysts supported on non-reducible MgO, the optimum molar metal composition Ni:Fe for CO_2 methanation was established to be 5:1. In

accordance with previous reports on the promoting role of Fe for methanation, an increase in activity and CH_4 selectivity was observed, however, the selectivity around 10% at 350 °C was still low and the activity was not stable. An increased reaction order of H_2 and CO_2 in methanation with the addition of Fe further confirmed the promoting effect, which was not observed for the RWGS reaction.

2. The optimal ratio of Ni:Fe = 5:1 was further introduced to bimetallic Ni,Fe catalysts supported on CeO_2 and ZrO_2 and compared to monometallic counterparts to investigate the combined role of promoter and support effects for these two reducible oxides. CeO_2 was the most active support for both methanation and RWGS reactions, followed by ZrO_2, while MgO-supported bimetallic catalyst showed the lowest catalytic performance. This order corresponds to the reducibility of the supports suggesting metal-support interaction as origin of this effect. On these reducible supports, the presence of Fe even resulted in a bit lower methanation activity while the RWGS reaction was slightly promoted on both CeO_2 and ZrO_2 supported Ni,Fe catalysts. Therefore, different from the non-reducible MgO-supported catalysts, no promoting effect of Fe for methanation was observed on reducible oxides. This can be explained following the explanation of the promoting effect by Grundwaldt et al., who proposed that the redox cycle of Fe at the surface of the Ni particles helps the CO_2 activation. In case of reducible oxides such as ZrO_2 or CeO_2 such activation of CO_2 can happen on oxygen vacancies of the support, and thus no promotion on the metal surface might be required. It was shown previously that oxygen vacancies and metal-zirconia interfacial sites can promote the activation of CO_2.[5, 34, 38] Such synergistic interplay of reduced oxide sites for CO_2 activation and metal

sites for H_2 activation can also explain the superior stability of the catalysts supported on reducible oxides as no or less carbon species or oxygen-containing coupled products are present on the metal surface leading to deactivation by coking or oxidation.

3. ZrO_2-supported catalysts exhibited the highest CH_4 selectivity (94.4% on Ni/ZrO_2 at 350 °C). Instead of deactivation, they also showed a long activation period (~10 h) during reaction, consistent with the slow formation of oxygen vacancies due to the moderate reducibility. Also, the kinetic parameters were standing out from the other catalysts with regard to a very high activation energy and a strongly negative reaction order of H_2 for RWGS. In the context of our interpretation, this suggests that CO_2 competes with H_2 for the adsorption sites on the metallic Ni surface. Due to the hydrogen-rich feed stoichiometry, RWGS is inhibited by hydrogen and only little carbonaceous intermediates might be present on the Ni particles. The preferred CO_2 activation on the reduced support sites on the other hand does not lead to CO pathway on the metal sites likely proceeds via formate pathway on support sites with adjacent oxygen vacancies to form methane.[41, 78]

4. The *in situ* DRIFTS results demonstrate that MgO, ZrO_2 and CeO_2 have a strong influence on Ni active sites. More specifically, there is a clear difference in the CO_{ad} species formed. The intensity ratio between carbonaceous / carbonates-like species and CO_{ad} bands on each sample after steady-state CO adsorption increased with increasing of the support reducibility (Figure 12d), which can be interpreted as the Boudouard reaction is more promoted by the presence of oxygen vacancies. Such disproportionation will result carbon layer covered on Ni and prevent the formation of CO_{ad}. The other

disproportionation product CO_2 will then be adsorbed on the support, which is consistent

with our kinetic analysis. All these findings highlight MSI in reducible oxide-supported

Ni-based catalysts, which can be addressed for the difference in their catalytic

performance.

5. Conclusion

In conclusion, this study has shown that the well-established promotion effect of Fe on

Ni-based catalysts with similar metal loading and metal particle size is present if

non-reducible MgO is used as support, which according to literature report can be traced back

to facilitated CO_2 activation involving Fe redox cycles. If reducible supports such as ZrO_2

and CeO_2 are involved, no such effect is evident. *In situ* DRIFTS with CO as probe and

H_2-TPR as well as CO_2-TPD have demonstrated that the importance of MSI effect in these

two supports, resulting into a new mechanism of CO_2 activation on the supports and

rendering a promotion on the metal surface by Fe redundant. This hypothesis is consistent

with the kinetic parameters reported here, which are most pronounced on Ni/ZrO_2, i.e. a large

activation energy and a negative reaction order for H_2 in RWGS, while the pre-factor for

methanation was still large. For these reasons, Ni/ZrO_2 reached the highest CH_4 selectivity of

94% at 350 °C, which is accompanied by an interesting activation behavior due to the

dynamic nature of the under-lying MSI. The catalysts supported on the most reducible oxide

CeO_2 with the richest oxygen vacancies showed the highest CO_2 methanation activity.

Nanoscale Accepted Manuscript

References:

1. H. Blanco and A. Faaij, *Renew. Sustain. Energy Rev.*, 2018, **81**, 1049-1086.

2. X. Ning, R. Lin, R. O'Shea, D. Wall, C. Deng, B. Wu and J. D. Murphy, *Iscience*, 2021, **24**.

3. A. Antenucci and G. Sansavini, *Renew. Sustain. Energy Rev.*, 2019, **100**, 33-43.

4. R. Estevez, L. Aguado-Deblas, F. M. Bautista, F. J. López-Tenllado, A. A. Romero and D. Luna, *Catal.*, 2022, **12**, 1555.

5. H. Chen, H. Cui, Y. Lv, P. Liu, F. Hao and W. Xiong, *Fuel*, 2022, **314**, 123035.

6. R.-P. Ye, J. Ding, W. Gong, M. D. Argyle, Q. Zhong, Y. Wang, C. K. Russell, Z. Xu, A. G. Russell, Q. Li, M. Fan and Y.-G. Yao, *Nat. Commun.*, 2019, **10**, 5698.

7. L. Li, W. Zeng, M. Song, X. Wu, G. Li and C. Hu, *Catal.*, 2022, **12**, 244.

8. N. D. Mohd Ridzuan, M. S. Shaharun, M. A. Anawar and I. Ud-Din, *Catal.*, 2022, **12**, 469.

9. M. A. Aziz, A. A. Jalil, N. S. Hassan, M. Bin Bahari, A. H. Hatta, T. A. T. Abdullah, N. W. C. Jusoh, H. D. Setiabudi and R. Saravanan, *Process Saf. Environ. Prot.*, 2024, **186**, 1229-1241.

10. S. Chen and A. M. Abdel-Mageed, *Int. J. Hydrogen Energy*, 2023, **48**, 24915-24935.

11. E. Spennati, P. Riani and G. Garbarino, *Catal. Today*, 2023, **418**, 114131.

12. M. Tawalbeh, R. Muhammad Nauman Javed, A. Al-Othman and F. Almomani, *Energy Convers. Manag.*, 2023, **279**, 116755.

13. J. Sehested, K. E. Larsen, A. L. Kustov, A. M. Frey, T. Johannessen, T. Bligaard, M. P. Andersson, J. K. Nørskov and C. H. Christensen, *Top. Catal.*, 2007, **45**, 9-13.

14. Y. Feng, L. Shen, W. Zhang, X. Yuan, M. Zhu and J. Xu, *J. CO2 Util.*, 2024, **80**, 102683.

15. A. I. Tsiotsias, N. D. Charisiou, I. V. Yentekakis and M. A. Goula, in *Nanomater.*, 2021, vol. 11.

16. A. L. Kustov, A. M. Frey, K. E. Larsen, T. Johannessen, J. K. Nørskov and C. H. Christensen, *Appl. Catal. A-Gen.*, 2007, **320**, 98-104.

17. Z. Bian, S. Das, M. H. Wai, P. Hongmanorom and S. Kawi, *ChemPhysChem*, 2017, **18**, 3117-3134.

18. T. Pu, J. Chen, W. Tu, J. Xu, Y.-F. Han, I. E. Wachs and M. Zhu, *J. Catal.*, 2022, **413**, 821-828.

19. J. Li, Q. Xu, Y. Han, Z. Guo, L. Zhao, K. Cheng, Q. Zhang and Y. Wang, *Sci. China Chem.*, 2023, **66**, 3518-3524.

20. M.-A. Serrer, A. Gaur, J. Jelic, S. Weber, C. Fritsch, A. H. Clark, E. Saraçi, F. Studt and J.-D. Grunwaldt, *Catal. Sci. Technol.*, 2020, **10**, 7542-7554.

21. M.-A. Serrer, K. F. Kalz, E. Saraçi, H. Lichtenberg and J.-D. Grunwaldt, *ChemCatChem*, 2019, **11**, 5018-5021.

22. B. Mutz, M. Belimov, W. Wang, P. Sprenger, M.-A. Serrer, D. Wang, P. Pfeifer, W. Kleist and J.-D. Grunwaldt, *ACS Catal.*, 2017, **7**, 6802-6814.

23. A. B. Shirsath, M. L. Schulte, B. Kreitz, S. Tischer, J.-D. Grunwaldt and O. Deutschmann, *Chem. Eng. J.*, 2023, **469**, 143847.

24. H. L. Huynh, J. Zhu, G. Zhang, Y. Shen, W. M. Tucho, Y. Ding and Z. Yu, *J. Catal.*, 2020, **392**, 266-277.

25. B. Yan, B. Zhao, S. Kattel, Q. Wu, S. Yao, D. Su and J. G. Chen, *J. Catal.*, 2019, **374**, 60-71.

26. Z. Zhang, C. Shen, K. Sun, X. Jia, J. Ye and C.-j. Liu, *J. Mater. Chem. A*, 2022, **10**, 5792-5812.

27. W. K. Fan and M. Tahir, *J. Environ. Chem. Eng.*, 2021, **9**, 105460.

28. Q. Li, C. Wang, H. Wang, J. Chen, J. Chen and H. Jia, *Angew. Chem. Int. Ed.*, 2024, **136**, e202318166.

29. C. Vogt, E. Groeneveld, G. Kamsma, M. Nachtegaal, L. Lu, C. J. Kiely, P. H. Berben, F. Meirer and B. M. Weckhuysen, *Nat. Catal.*, 2018, **1**, 127-134.

30. X. Zhou, G. A. Price, G. J. Sunley and C. Copéret, *Angew. Chem. Int. Ed.*, 2023, **62**, e202314274.

Nanoscale Accepted Manuscript

31. W. Gac, W. Zawadzki, M. Rotko, M. Greluk, G. Słowik and G. Kolb, *Catal. Today*, 2020, **357**, 468-482.

32. P. Frontera, A. Macario, M. Ferraro and P. Antonucci, in *Catal.*, 2017, vol. 7.

33. L. P. Matte, A. S. Kilian, L. Luza, M. C. M. Alves, J. Morais, D. L. Baptista, J. Dupont and F. Bernardi, *J. Phys. Chem. C*, 2015, **119**, 26459-26470.

34. K. Larmier, W.-C. Liao, S. Tada, E. Lam, R. Verel, A. Bansode, A. Urakawa, A. Comas-Vives and C. Copéret, *Angew. Chem. Int. Ed.*, 2017, **56**, 2318-2323.

35. R. Ye, L. Ma, X. Hong, T. R. Reina, W. Luo, L. Kang, G. Feng, R. Zhang, M. Fan and R. Zhang, *Angew. Chem. Int. Ed.*, 2024, **136**, e202317669.

36. Y. Ding, J. Chen, X. Lian, Z. Tian, X. Geng, Y. Wang, Y. Liu, W. Wang, M. Wang and Y. Xiao, *Appl. Catal. B-Environ.*, 2024, **343**, 123508.

37. M. A. Abir, R. E. Phillips, J. Z. M. Harrah and M. Ball, *Catal. Sci. Technol.*, 2024.

38. S. Kumari, A. N. Alexandrova and P. Sautet, *J. Am. Chem. Soc.*, 2023, **145**, 26350-26362.

39. S. Chen, A. M. Abdel-Mageed, C. Gauckler, S. E. Olesen, I. Chorkendorff and R. J. Behm, *J. Catal.*, 2019, **373**, 103-115.

40. Y. Bian, C. Xu, X. Wen, L. Xu, Y. Cui, S. Wang, C.-e. Wu, J. Qiu, G. Cheng and M. Chen, *Fuel*, 2023, **331**, 125755.

41. F. Arena, G. Italiano, K. Barbera, S. Bordiga, G. Bonura, L. Spadaro and F. Frusteri, *Appl. Catal. A-Gen.*, 2008, **350**, 16-23.

42. M. Monai, K. Jenkinson, A. E. M. Melcherts, J. N. Louwen, E. A. Irmak, S. Van Aert, T. Altantzis, C. Vogt, W. van der Stam, T. Duchoň, B. Šmíd, E. Groeneveld, P. Berben, S. Bals and B. M. Weckhuysen, *Science*, 2023, **380**, 644-651.

43. C. Wei, H. Ding, Z. Zhang, F. Lin, Y. Xu and W. Pan, *Int. J. Hydrogen Energy*, 2024, **58**, 872-891.

44. F. Hu, C. Jin, K. H. Lim, C. Li, G. Song, Bella, T. Wang, R. Ye, Z.-H. Lu, G. Feng, R. Zhang and S. Kawi, *Fuel Process. Technol.*, 2023, **250**, 107873.

45. G. S. Dhillon, G. Cao and N. Yi, in *Catal.*, 2023, vol. 13.

46. W. L. Vrijburg, J. W. A. van Helden, A. Parastaev, E. Groeneveld, E. A. Pidko and E. J. M. Hensen, *Catal. Sci. Technol.*, 2019, **9**, 5001-5010.

47. M. Jafarbegloo, A. Tarlani, A. W. Mesbah, J. Muzart and S. Sahebdelfar, *Catal. Letters*, 2016, **146**, 238-248.

48. L. Geng, B. Zheng, X. Wang, W. Zhang, S. Wu, M. Jia, W. Yan and G. Liu, *ChemCatChem*, 2016, **8**, 805-811.

49. Y. Wei, D. Luo, L. Yan, C. Ma, Z. Fu, L. Guo, M. Cai, S. Sun and C. Zhang, *Catal. Letters*, 2022, **152**, 1835-1843.

50. C. Mebrahtu, S. Perathoner, G. Giorgianni, S. Chen, G. Centi, F. Krebs, R. Palkovits and S. Abate, *Catal. Sci. Technol.*, 2019, **9**, 4023-4035.

51. J. Li, J. Li and Q. Zhu, *Chin. J. Chem. Eng.*, 2018, **26**, 2344-2350.

52. D. Weber, T. He, M. Wong, C. Moon, A. Zhang, N. Foley, N. J. Ramer and C. Zhang, *Catal.*, 2021, **11**, 1447.

53. C. Janke, M. S. Duyar, M. Hoskins and R. Farrauto, *Appl. Catal. B-Environ.*, 2014, **152**, 184-191.

54. N. L. Visser, S. J. Turner, J. A. Stewart, B. D. Vandegehuchte, J. E. S. van der Hoeven and P. E. de Jongh, *ACS Nano*, 2023, **17**, 14963-14973.

55. P. Munnik, M. E. Z. Velthoen, P. E. de Jongh, K. P. de Jong and C. J. Gommes, *Angew. Chem. Int. Ed.*, 2014, **126**, 9647-9651.

Nanoscale Accepted Manuscript

56. M. Mihaylov, K. Hadjiivanov and H. Knözinger, *Catal. Letters*, 2001, **76**, 59-63.

57. M. Agnelli, H. M. Swaan, C. Marquez-Alvarez, G. A. Martin and C. Mirodatos, *J. Catal.*, 1998, **175**, 117-128.

58. N. Liu, J. Wei, J. Xu, Y. Yu, J. Yu, Y. Han, K. Wang, J. I. Orege, Q. Ge and J. Sun, *Appl. Catal. B-Environ.*, 2023, **328**, 122476.

59. L. Li, B. Jiang, D. Tang, Z. Zheng and C. Zhao, in *Catal.*, 2018, vol. 8.

60. W. Yu, Q. Zhou, H. Wang, Y. Liu, W. Chu, R. Cai and W. Yang, *J. Mater. Sci.*, 2020, **55**, 2321-2332.

61. X. Zhang, R. You, D. Li, T. Cao and W. Huang, *ACS Appl. Mater. Interfaces.*, 2017, **9**, 35897-35907.

62. Y. Gao, R. Li, S. Chen, L. Luo, T. Cao and W. Huang, *Phys. Chem. Chem. Phys.*, 2015, **17**, 31862-31871.

63. W. Zheng, J. Zhang, Q. Ge, H. Xu and W. Li, *Appl. Catal. B-Environ.*, 2008, **80**, 98-105.

64. T. Takeguchi, S.-n. Furukawa and M. Inoue, *J. Catal.*, 2001, **202**, 14-24.

65. C. Li, Y. Shi, Z. Zhang, J. Ni, X. Wang, J. Lin, B. Lin and L. Jiang, *J. Energy Chem.*, 2021, **60**, 403-409.

66. K. Chang, H. Zhang, M.-j. Cheng and Q. Lu, *ACS Catal.*, 2020, **10**, 613-631.

67. M. Carltonbird, S. Eaimsumang, S. Pongstabodee, S. Boonyuen, S. M. Smith and A. Luengnaruemitchai, *Chem. Eng. J.*, 2018, **344**, 545-555.

68. X. Li, X. Liu, J. Hao, L. Li, Y. Gao, Y. Gu, Z. Cao and J. Liu, *ACS Omega*, 2022, **7**, 24646-24655.

69. A. Parastaev, V. Muravev, E. Huertas Osta, A. J. F. van Hoof, T. F. Kimpel, N. Kosinov and E. J. M. Hensen, *Nat. Catal.*, 2020, **3**, 526-533.

70. L. R. Winter, E. Gomez, B. Yan, S. Yao and J. G. Chen, *Appl. Catal. B-Environ.*, 2018, **224**, 442-450.

71. B. Miao, S. S. K. Ma, X. Wang, H. Su and S. H. Chan, *Catal. Sci. Technol.*, 2016, **6**, 4048-4058.

72. S. Chen, A. M. Abdel-Mageed, M. Li, S. Cisneros, J. Bansmann, J. Rabeah, A. Brückner, A. Groß and R. J. Behm, *J. Catal.*, 2021, **400**, 407-420.

73. X. Jia, X. Zhang, N. Rui, X. Hu and C.-j. Liu, *Appl. Catal. B-Environ.*, 2019, **244**, 159-169.

74. Z. Cheng, B. J. Sherman and C. S. Lo, *J. Chem. Phys.*, 2013, **138**.

75. K. Lorber, J. Zavašnik, I. Arčon, M. Huš, J. Teržan, B. Likozar and P. Djinović, *ACS Appl. Mater. Interfaces.*, 2022, **14**, 31862-31878.

76. N. Rui, X. Zhang, F. Zhang, Z. Liu, X. Cao, Z. Xie, R. Zou, S. D. Senanayake, Y. Yang, J. A. Rodriguez and C.-J. Liu, *Appl. Catal. B-Environ.*, 2021, **282**, 119581.

77. T. Zhang, W. Wang, F. Gu, W. Xu, J. Zhang, Z. Li, T. Zhu, G. Xu, Z. Zhong and F. Su, *Appl. Catal. B-Environ.*, 2022, **312**, 121385.

78. K. Li and J. G. Chen, *ACS Catal.*, 2019, **9**, 7840-7861.

79. J. I. Di Cosimo, Apesteguı, C. R.́ a, M. J. L. Ginés and E. Iglesia, *J. Catal.*, 2000, **190**, 261-275.

80. D. Wierzbicki, R. Baran, R. Dębek, M. Motak, T. Grzybek, M. E. Gálvez and P. Da Costa, *Int. J. Hydrogen Energy*, 2017, **42**, 23548-23555.

81. P. Summa, M. Gajewska, L. Li, C. Hu, B. Samojeden, M. Motak and P. Da Costa, *J. CO2 Util.*, 2022, **60**, 101983.

82. N. J. A. Rahman, A. Ramli, K. Jumbri and Y. Uemura, *Sci. Rep.*, 2019, **9**, 16223.

83. Z. Ni, X. Djitcheu, X. Gao, J. Wang, H. Liu and Q. Zhang, *Sci. Rep.*, 2022, **12**, 5344.

84. W. Liao, C. Tang, H. Zheng, J. Ding, K. Zhang, H. Wang, J. Lu, W. Huang and Z. Zhang, *J. Catal.*, 2022, **407**, 126-140.

85. Y. Wang, H. Ban, Y. Wang, R. Yao, S. Zhao, J. Hu and C. Li, *J. Catal.*, 2024, **430**, 115357.

86. S. Lin, Z. Li and M. Li, *Fuel*, 2023, **333**, 126369.

87.   M. B. Jensen, L. G. M. Pettersson, O. Swang and U. Olsbye, *J.Phys.Chem.B*, 2005, **109**, 16774-16781.

88.   D. Cornu, H. Guesmi, J.-M. Krafft and H. Lauron-Pernot, *J.Phys.Chem.C*, 2012, **116**, 6645-6654.

89.   R. Ye, L. Ma, X. Hong, T. R. Reina, W. Luo, L. Kang, G. Feng, R. Zhang, M. Fan, R. Zhang and J. Liu, *Angew. Chem. Int. Ed.*, 2024, **136**, e202317669.

90.   Y. Yang, Z. Chai, X. Qin, Z. Zhang, A. Muhetaer, C. Wang, H. Huang, C. Yang, D. Ma, Q. Li and D. Xu, *Angew. Chem. Int. Ed.*, 2022, **61**, e202200567.

91.   I. Hussain, G. Tanimu, S. Ahmed, C. U. Aniz, H. Alasiri and K. Alhooshani, *Int. J. Hydrogen Energy*, 2023, **48**, 24663-24696.

92.   B. M. Tackett, E. Gomez and J. G. Chen, *Nat. Catal.*, 2019, **2**, 381-386.

93.   A. Beck, D. Kazazis, Y. Ekinci, X. Li, E. A. Müller Gubler, A. Kleibert, M.-G. Willinger, L. Artiglia and J. A. van Bokhoven, *ACS Nano*, 2023, **17**, 1091-1099.

94.   C. Ren, R. Yang, Y. Li and H. Wang, *Rev. Chem. Intermed.*, 2019, **45**, 3019-3032.

95.   K. I. Hadjiivanov and G. N. Vayssilov, 2002.

96.   G. Martra, F. Arena, M. Baricco, S. Coluccia, L. Marchese and A. Parmaliana, *Catal. Today*, 1993, **17**, 449-458.

97.   K. I. Hadjiivanov and G. N. Vayssilov, in *Adv. Catal.*, Academic Press, 2002, vol. 47, pp. 307-511.

98.   G. Busca and V. Lorenzelli, *Mater. Chem.*, 1982, **7**, 89-126.

99.   S. Chen, T. Cao, Y. Gao, D. Li, F. Xiong and W. Huang, *J.Phys.Chem.C*, 2016, **120**, 21472-21485.

100. S. Chen, L. Luo, Z. Jiang and W. Huang, *ACS Catal.*, 2015, **5**, 1653-1662.

101. M. B. Jensen, S. Morandi, F. Prinetto, A. O. Sjåstad, U. Olsbye and G. Ghiotti, *Catal. Today*, 2012, **197**, 38-49.

Nanoscale Accepted Manuscript

The data supporting this article have been included as part of the Supplementary Information.

Nanoscale Accepted Manuscript